Chapter

Tribological Performance of Random Sinter Pores vs. Deterministic Laser Surface Textures: An Experimental and Machine Learning Approach

Guido Boidi, Philipp G. Grützmacher, Markus Varga, Márcio Rodrigues da Silva, Carsten Gachot, Daniele Dini, Francisco J. Profito and Izabel F. Machado

Abstract

This work critically scrutinizes and compares the tribological performance of randomly distributed surface pores in sintered materials and precisely tailored laser textures produced by different laser surface texturing techniques. The pore distributions and dimensions were modified by changing the sintering parameters, while the topological features of the laser textures were varied by changing the laser sources and structuring parameters. Ball-on-disc tribological experiments were carried out under lubricated combined sliding-rolling conditions. Film thickness was measured *in-situ* through a specific interferometry technique developed for the study of rough surfaces. Furthermore, a machine learning approach based on the radial basis function method was proposed to predict the frictional behavior of contact interfaces with surface irregularities. The main results show that both sintered and laser textured materials can reduce friction compared to the untextured material under certain operating conditions. Moreover, the machine learning model was shown to predict results with satisfactory accuracy. It was also found that the performance of sintered materials could lead to similar improvements as achieved by textured surfaces, even if surface pores are randomly distributed and not precisely controlled.

Keywords: lubrication, friction reduction, laser surface texturing, sintered material, machine learning

1. Introduction

The surface topography of mechanical components is often modified to improve their tribological performance, such as cylinder liner honing in internal combustion engines [1] and laser surface texturing in piston-rings [2, 3], rolling element bearings [4], and journal- and thrust bearing systems [5].

Surface textures can promote several tribological improvements. Surface cavities can reduce abrasive wear in harsh contact conditions by retaining wear and contaminant particles (debris trapping effect), as well as work as micro-reservoirs and secondary oil suppliers (oil reservoir effect) [6]. Under mixed and (elasto) hydrodynamic lubrication, friction can be reduced by the interplay of different mechanisms, such as the (i) micro-hydrodynamic bearing (boosting in the fluid pressures due to the texture-induced cavitation at the divergent regions of the textures) [7], (ii) inlet suction (lubricant sucking into the interface due to the difference between the supply pressure and the cavitation pressure) [3, 8, 9], and (iii) shear-area variation (decrease of the fluid and contact shear stresses over the contact area) [10] mechanisms. Furthermore, under boundary and mixed lubrication regimes, textures can influence the sealing performance and percolation behavior. The reader is referred to the comprehensive reviews [4, 11–14] for a more in-depth evaluation of several aspects of surface texturing for tribological improvements.

The tribological effects of surface texturing were first studied in the 1960s by Hamilton's and Anno's research groups [15, 16]. Afterwards, this topic covered a marginal role in the tribological community until the 1990s, when Etsion and co-workers re-discovered its potential impact [17, 18], also in the context of improved manufacturing techniques. In recent years, the interest in research on surface texturing, mainly laser texturing, has significantly increased [11] as some texture configurations have shown significant tribological improvements in various machine elements [2, 19–21].

The design of effective surface textures requires a thorough understanding of the tribosystem's characteristics and the capabilities and limitations of the texturing techniques available. General guidelines for texture design could be found in [4, 12]. Nevertheless, further in-depth research is still required to reveal the precise mechanisms (and their interplay) responsible for the improvements in tribological performance due to the presence of optimally designed micro-textured surfaces; this is still not fully understood. This lack of understanding is mainly related to the design and manufacturing limitations of optimal texture geometries for different components, the influence of varying operating conditions in transient applications, and the evolution of the texture geometry over the components' lifetime. Additionally, there is a particular debate on the effect of surface textures on the behavior of lubricated non-conformal contacts under different sliding-rolling conditions. Finally, to successfully and economically implement surface texturing in practical applications and industrial scale, the gain in tribological performance must compensate for the additional manufacturing steps leading to longer processing times and costs.

Surface porosity in sintered materials could be potentially used as inherent surface texture and saving extra manufacturing. Pore characteristics can be controlled, to certain limits, by the sintering parameters and powder properties [22]. However, in contrast to deterministic laser textures – with a precisely tailored topography – surface pores are statistically distributed and have irregular shapes. The effect of pores on mechanical proprieties of sintered materials was extensively studied [23–26]; however, the influence of surface porosity on the tribological performance is sparsely investigated [27–29].

Advanced statistics, artificial intelligence (AI) and machine learning (ML) methods have gained increasing importance in describing and interpreting scientific findings. In tribology research, ML & AI approaches have already been used for online condition monitoring of bearings, design of material composition, lubricant formulations, lubrication and fluid film formation analysis, among other applications [30–32]. An ML method was also recently proposed to predict the frictional performance of textured and porous interfaces [33], whose methodology could be extended to support the optimum design of surface texturing.

This study aims to quantitatively compare random surface features of porous sintered materials with distinctly manufactured laser surface textures in the particular case of lubricated non-conformal contacts. Especially the sliding-rolling conditions as occurring in roller-bearings are tackled. Finally, the radial basis ML method was used to enhance results interpretation and build a general predictive model to support the design of new surface features for obtaining superior tribological performances.

2. Sample manufacturing and surface texturing

The geometries of the sintered and laser textured samples had either curved surfaces (ball-shape) or plain surfaces (face of the disc). The geometrical dimension of samples followed standard dimensions imposed by the tribometer manufacturer, see Section 3. Balls are ø19.05 mm and discs ø46 × 6 mm.

Reference steel material (AISI 52100), defined as NP (Non-Porous), was used as the benchmark for comparing the results obtained from surface modifications (both from randomly distributed surface pores and deterministic laser textures). NP samples were purchased from the test rig manufacturer with controlled roughness (Sq = 20 nm) and dimensions; therefore, no further operations were needed. Samples with surface features (either pores or texture) were always tested against reference NP material (either ball or disc). Sintered against sintered (or textured against textured) condition was avoided to facilitate results interpretations and isolate the effect of surface features. The sintering process for powder metallurgy (PM) samples was followed by machining to obtain the final sample geometry, whereas laser texturing was directly applied on reference steel samples present in the final geometry for testing.

2.1 Powder metallurgy, sintering techniques and porosity

Powder metallurgy (PM) refers to the conjunction of processes and operations for obtaining components from powders mixtures through a sintering process. The drive for sintering is the reduction of free energy between particles and consequently diffusion during sintering [34, 35]. Details of conventional PM processes are out of the scope of this work and can be found in [22].

Besides them, Spark Plasma Sintering (SPS) [36] has attracted attention in the last decades [37–41] due to high densification achieved in reduced time and grain grow inhibition [42–44], as SPS is a pressure-assisted process. The powder mixtures are placed in an electrically conductive die (often graphite) that is mounted in a low vacuum chamber. Two graphite punches apply load on the die and permit a pulsed electric current passage that increases samples' temperature and enhances sintering. SPS also allows high heating rates (up to 100 °C/min), and is applied to reduce porosity and improve densification [45, 46]. SPS' monitoring and controlling system of temperature and pressure allow obtaining materials with a range of densifications and compositions. Hence, SPS makes it possible to tailor and prototype different materials [47].

Pores strongly influence mechanical and tribological properties of sintered samples [23, 26, 28, 41, 48]. Therefore, precise control and characterization of pores are required in PM. The quantity and characteristics of pores depend either on powder characteristics (shape, dimensions, distribution, particle mechanical properties) or on the sintering processes and parameters (pressure, sintering time and temperature) [36]. Particles with similar size distribution and irregular shape improve densification during the compacting phase and reduce porosity in the final components [36]. Similarly, increasing the applied pressure reduces total porosity. Pore characteristics including area, size, perimeter, average distance between pores, distribution and shape can be controlled by sintering temperature and time. The increase of sintering temperature promotes diffusion and increases densification, reduces total porosity, pore dimensions and irregular shape [27, 49], and the occurrence of grain growth. Archimedes' method [50] can estimate the total porosity, and pore characteristics can be evaluated through image analysis. In this study, images were taken in five different areas on the sintered samples' surface and then processed using the freely available Image J software [51] to highlight and characterize the pores. Only pore size and circularity index were considered here as main factors [52]. The circularity index ranges between 0 (very irregular) and 1 (perfectly circular) [52].

Surface roughness is another crucial parameter that strongly influences the tribological performance of tribosystems. For PM materials, roughness evaluation is not trivial since pores represent geometrical depressions that significantly increase the root mean square roughness (*Sq*) of the surfaces. Alternatively, the *plateau* root mean square roughness (*Spq*) parameter generally used to characterize honed cylinder liner topographies [53–55] is adopted to quantify the roughness of PM samples. Besides, an *ad-hoc* measuring and postprocessing procedure, including the choice of the roughness filter and cut-off values), was developed to weakening pore contours' effects on roughness characterization. More details of this procedure can be found in previous publications [29, 56–58]. The surface roughness of the reference smooth material NP was evaluated using the *Sq* parameter.

For this study, a commercially available steel powder mixture (Astaloy85Mo) was used. The Fe-based mixture contains 0.85 wt.% Mo, 0.3 wt.% C. Ball-shape samples were manufactured via SPS, whereas disc-shaped samples via conventional sintering. As SPS only generates cylinders and conventional sintering produced some surface irregularities, ball and disc samples had to be machined to achieve the final geometry for testing. All sintered samples were water quenched at 850°C and polished.

Different sintering parameters were used for varying porosity, see **Table 1**. Only one sintering condition is presented for the ball-shaped samples as this set of parameters (Ball-Sint) was the only one where open surface pores could be observed after machining [29, 56]. Three different compacting pressures were used with the conventional sintering technique for obtaining disc samples with different porosity. The main characteristics of sintered materials are summarized in **Table 2**.

2.2 Laser texturing techniques

As laser surface texturing is the technique most successfully used to apply deterministic textures on engineering surfaces [59], it was chosen to compare

	Sintered balls	Sintered discs		
	SPS	Conventional Sintering		
	Ball-Sint	Disc-Si4	Disc-Si5	Disc-Si6
Compacting pressure (MPa)	35	400	500	600
Sintering temperature (°C)	800	1280	1280	1280
Holding time (min)	1	60	60	60

Table 1.
Sintering parameters used to manufacture the ball (SPS technique) and disc samples (conventional sintering).

	Sintered balls	Sintered discs			Discs/balls
	Ball-Sint	**Disc-Si4**	**Disc-Si5**	**Disc-Si6**	**NP**
Density (g/cm^3)	6.6	6.7	6.9	7.0	7.8
Surface porosity (%)	2	14	12	11	NA*
Average surface pore size (μm)	2.0	7.1	6.5	5.4	NA
Average circularity index (-)	0.9 ± 0.1	0.7 ± 0.3	0.8 ± 0.2	0.8 ± 0.2	NA
Surface hardness (HV1)	600 ± 80	520 ± 85	520 ± 75	550 ± 55	750 ± 25
Surface roughness, Sq (nm)	180 ± 50	370 ± 85	280 ± 70	190 ± 60	20 ± 5

**NA = not applicable.*

Table 2.
Porosity characteristics, Vickers hardness and surface roughness values of sintered and NP samples.

against sintered samples with random textures. Laser texturing of ball samples demonstrates the feasibility of processing curved surfaces, which is highly interesting for a wide range of applications (*i.e.* ball bearings). The texture design in terms of shape and dimensions is inspired by the most promising solutions from the literature [4, 11–14].

Two different laser systems were used to texture ball samples, which are based on different mechanisms of texture generation: an Nd:YAG laser (Quanta Ray Pro 290, Newport Spectra Physics) with a pulse duration of 10 ns and a passively mode-locked ultrashort-pulsed Ti:Sapphire laser (Spitfire Pro XP, Newport Spectra Physics) with a pulse duration of 100 fs. Due to the different pulse durations of the laser systems, the ablation mechanism varies. In the case of the ns-system, the pulse duration is long enough to melt the material leading to a different texture morphology as it is the case for the fs-system, where the pulse duration is so short that the material is directly ablated, thereby preventing melt formation and keeping the heat-affected zone at a minimum [60]. The fs-Ti:Sapphire laser, having a wavelength of 800 nm and a repetition rate of 1 kHz, was used in a direct laser writing (DLW) process. In this process, the laser beam is focused by a collective lens with a focal length of 100 mm onto the sample surface. The sample is moved by a rotation stage, thereby scanning the laser beam over the surface and generating the desired texture shape. One single shot of the laser produces a circular dimple with a diameter of 50 μm and a depth of 0.1 μm. To generate dimples (Ball-Di) or grooves (Ball-LG), the rotation speed of the stage was adapted. For higher speeds, individual laser shots hit the surface (dimples), and for lower speeds, individual laser shots are overlapping by 50%, thus producing a homogenous line pattern (longitudinally oriented with respect to the sliding direction) [61]. The accumulated laser fluences were 3.87 and 5.57 J/cm^2 for the dimples and the grooves, respectively.

Grooves with an orientation perpendicular to the sliding direction were generated with the ns-Nd:YAG laser in a direct laser interference patterning (DLIP) process. The laser had a wavelength of 355 nm and a repetition rate of 10 Hz. In the DLIP process, the primary laser beam exiting the laser is split up into two sub-beams by a beam splitter, which are then traveling through an optical setup guiding both beams to the sample surface. Upon overlapping of the two laser beams, a sinusoidal intensity distribution results from the interference of the beams. At the intensity maxima positions, the material is molten and removed, whereas the material stays virtually unchanged at the intensity minima positions, thus forming a groove-like texture. The laser fluence was kept constant at 1.29 J/cm^2 for all experiments. Due to the nature of the texture formation, textures of much smaller feature

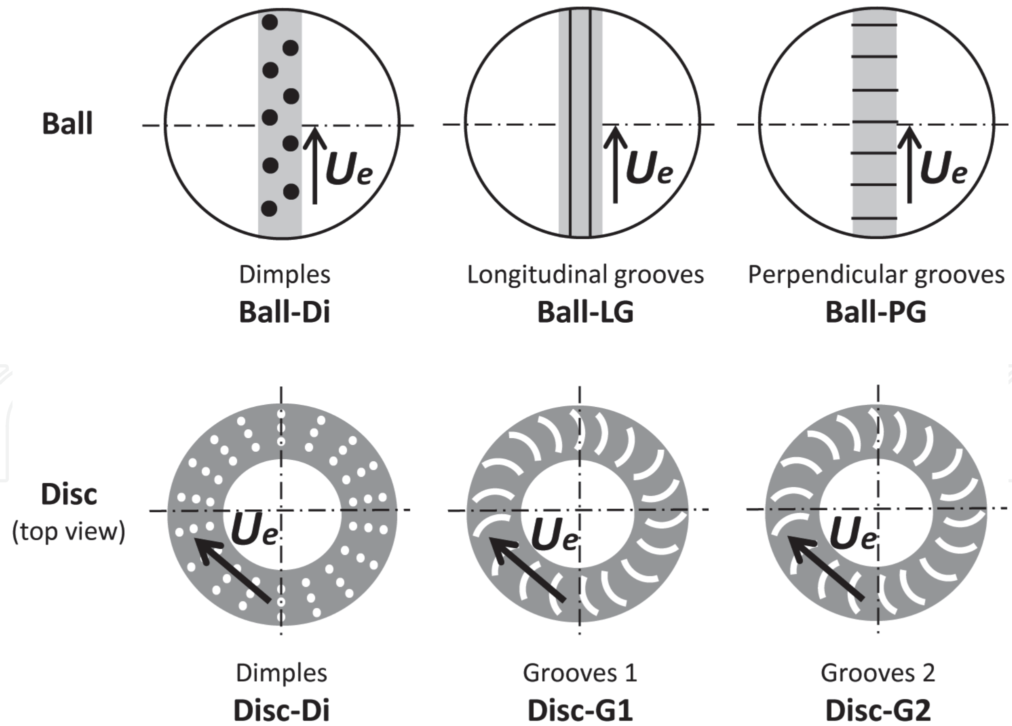

Figure 1.
Surface texture patterns on the ball and disc-shaped samples.

sizes are generated, and a higher processing speed can be achieved. Further details related to DLIP and the optical setup can be found in [62, 63].

The flat surface of disc-shaped samples was textured using another fs-laser system. Radial lines of dimples were designed along the tested circumference of the discs, see **Figure 1**. The dimples have a diameter of ~15 μm and a depth of 0.5 μm. The radial distance between dimples was maintained at 10 μm, and the circumferential distance between dimples is ~300 μm. Additionally, two configurations of curved radial grooves were designed on discs. One configuration of grooves had a shallow depth (<0.5 μm) compared to the other one (depth > 1 μm). The groove width was around 20 μm for both cases.

A schematic view of texture design on ball and disc samples is presented in **Figure 1**. The main geometrical characteristics of textured and sintered features are summarized and schematically represented in **Table 3** to facilitate the input into the ML algorithm (Section 5). Note that the coverage area (Ca) represents the percentage of texture area to the tested surface. The parameter P was introduced to evaluate the shape and orientation of the texture, and it was arbitrary assigned the values of 1 for perpendicular features, 0 for dimples and − 1 for longitudinal features.

3. Test rigs

3.1 Coefficient of friction measurements

The tribological tests were carried out in a ball-on-disc tribometer (MTM2 from PCS Instruments) under varying slide-to-roll ratio (SRR) conditions. In this tribometer, the ball and the disc are driven by two independent motors allowing continuous variations of SRR (see **Figure 2**). The coefficient of friction (COF) is calculated through the vertical load on the disc and the transversal force on the ball arm measured by load cells. The disc is mounted in a temperature-controlled bath, where a precise amount of lubricant is inserted. Another important feature of the test rig is the electric contact resistance (ECR) measurement. Although the ECR is

		Feature	Name	Schematic	W	D	C_a	C	P	Sq^*
					(μm)	(μm)	(%)	(%)	(−)	(μm)
Textured	**Ball**	Dimples	**Ball-Di**	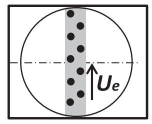	50	0.1	14	1	0	20
		Longitudinal Grooves	**Ball-LG**	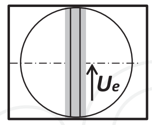	35	0.1	21	0	−1	20
		Perpendicular Grooves	**Ball-PG**	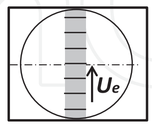	7	0.4	47	0	1	20
	Disc	Dimples	**Disc-Di**	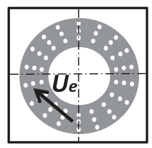	15	0.5	1	1	0	20
		Grooves 1	**Disc-G1**	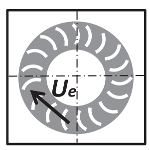	25	0.35	12.5	0	1	20
		Grooves 2	**Disc-G2**	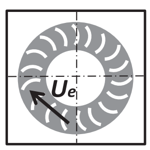	20	1.35	10	0	1	20
Sintered	**Ball**	Sintered	**Ball-Sint**	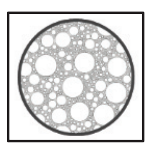	2	1	2	0.9	0	180
	Disc	Sintered-400 MPa	**Disc-Si4**	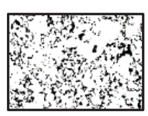	7	3.5	14	0.5	0	370
		Sintered-500 MPa	**Disc-Si5**	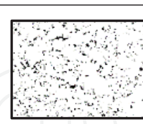	6	3	12	0.6	0	280
		Sintered-600 MPa	**Disc-Si6**	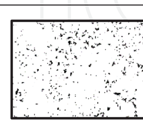	5	2.5	11	0.6	0	190

**Note that Spq was considered for sintered materials, whereas Sq was used for the smooth and textured samples.*

Table 3.
Schematic configuration and geometric characteristics of sintered and textured samples. W is the feature width, D feature depth, Ca is the coverage area, C circularity, P perpendicularity, and Sq is the surface roughness.

not a direct film thickness measurement, it enables identifying the lift-off speed, *i.e.* the minimum speed from which the contact surfaces are entirely separated by a thin film of lubricant [64].

Stribeck-like curves (COF *vs.* entrainment speed *Ue* at fixed SRR) were obtained at different SRRs for the sintered and textured materials. All tests were performed with synthetic base oil PAO6 at the constant temperature of 40 °C and constant maximum Hertzian pressure of 0.6 GPa. Each test was repeated three times to

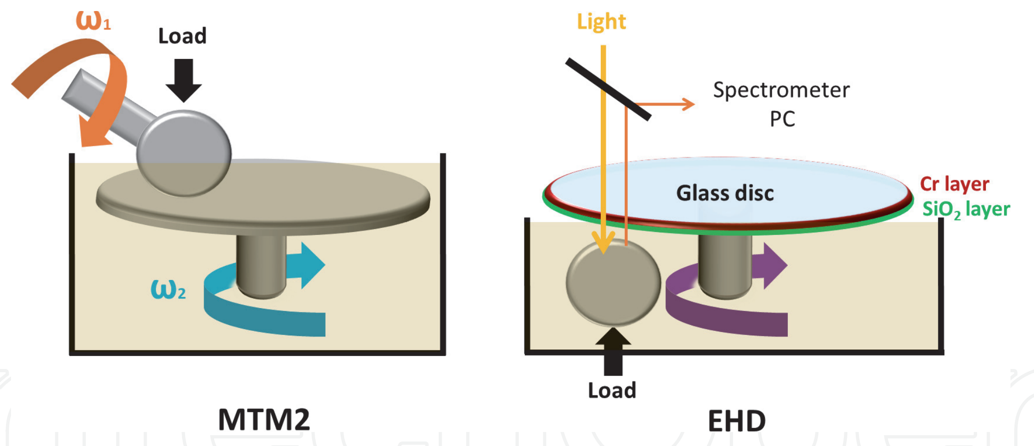

Figure 2.
Schematics of tribometers used for the coefficient of friction (MTM2) and film thickness measurements (EHD).

Parameter	*MTM 2*	*EHD*
Entrainment speed *Ue* (mm/s)	2000–10	2200–20
Side-to-roll-ratio SRR (%)	5–20 - 50 - 80 - 100 - 120 - 150 - 180	0
Temperature (°C)	40	40
Contact Pressure (GPa)	0.6	0.6
Lubricant	PAO6	PAO6

Table 4.
Test parameters adopted for friction (MTM2 rig) and film thickness (EHD rig) measurements.

assess repeatability. The detailed test parameters for the MTM2 rig are summarized in **Table 4**.

3.2 Film thickness measurements

The optical interferometry technique based on the spacer layer imaging method (SLIM) [65–67] was used for film thickness measurements. A steel ball is loaded against a glass disc coated with a Cr layer and a SiO_2 spacer layer (see **Figure 2**). Light passing through the disc is reflected by the ball surface and recombined by the light reflected by the Cr layer. Differences in light wavelength are used to calculate the central EHD lubricant film thickness of non-conformal contacts.

The used EHD test rig (PCS Instruments) with the SLIM setup had to be slightly modified for measuring film thickness on rough surfaces, according to Guegan [68–70]. Basically, this is achieved by two LED light sources to obtain brighter images, and the measurement is triggered to a specific ball position to always measure the film in the same position. Besides measuring central film thickness, the contact area and the minimum and maximum film thickness of a specific area can be calculated [68–70].

Only pure rolling (SRR 0%) was tested with this setup (see **Table 4**) since the increase of sliding may cause premature damage of the spacer layer, and it was proved that film thickness depends mainly on the entrainment speeds and only marginally on the SRR [69–71].

4. Experimental results and discussion

The authors have already published most of the experimental work for sintered [29, 37, 41, 57, 58] and textured materials [33, 56, 72, 73] presented in the following sections, and the main goal of this work is to provide a critical comparison between the different solutions. Hence, only the main results are reported and selected so that the tribological effects of surface pores and laser textures can be thoroughly evaluated and contrasted.

4.1 Sintered samples

Figure 3a shows the Stribeck-like curves of the sintered discs for SRR 100%. The results for distinct SRRs presented a similar trend. As can be observed, the decrease of total porosity and pore dimensions (**Table 2**) decreased the COF of the PM discs. The reduction of porosity goes conform with the decrement of surface roughness. As explained in Section 2.1, the alteration of surface pores is directly connected with surface morphology and, consequently, surface roughness. These parameters (surface roughness and porosity) should always be evaluated together when interpreting the friction results of PM materials.

Smooth reference samples NP showed significant lower COF when compared to the discs with pores. Again, this could be justified by the significant difference in surface roughness. For a better comparison between porous and NP samples, results can be evaluated in terms of the specific film thickness (Λ), see **Figure 3b**.

The sintered ball samples presented higher COF than NP for all SRRs and entrainment speeds, similarly to sintered discs. These outcomes are not explicitly

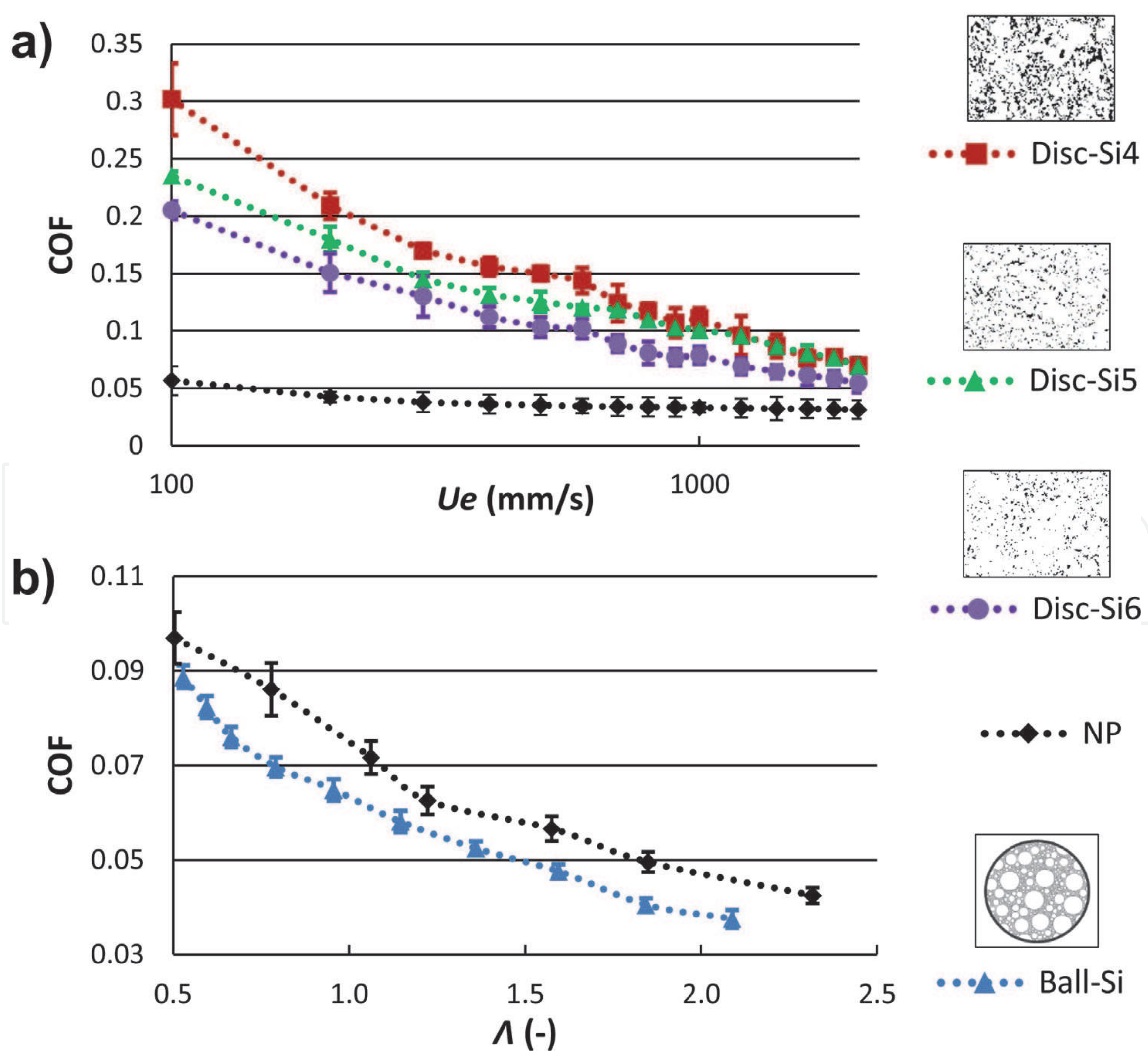

Figure 3.
a) Stribeck-like curves in terms of entrainment speed (COF vs. Ue) of sintered discs for SRR 100% and b) in terms of measured specific film thickness (COF vs. Λ) of NP and sintered balls for SRR 100%.

reported here and the reader is referred to the original reference for a more in-depth result examination [29]. As for the sintered disc, the improved performance of NP compared to sintered balls could be attributed to the significant difference in surface roughness of almost one order of magnitude between the two sets of samples (see **Table 2**).

Film thickness was only evaluated for the sintered (Ball-Sint) and NP balls. The optical interferometry technique requires glass discs, which excludes the use of sintered discs. The central region of every interferogram was selected, and the mean film thickness was analysed. The COF results of NP and sintered balls were compared in **Figure 3b** as a function of Λ for SRR 100%. As can be seen, the COF of sintered balls was lower than the NP samples for all Λ values, indicating beneficial friction behavior promoted by the surface porosity. Although only results for SRR 100% are shown here, this trend was also confirmed for other SRRs. These results show how surface pores can potentially have a similar effect as classical surface texturing. It should be noted that NP was tested at lower speeds than Ball-Sint for obtaining the COF in the same ranges; therefore, the increase of porosity and roughness in porous samples increased the lift-off speed compared to smooth NP surfaces.

Previous work by Li *et al.* [74] proved that the tribological behavior of PM materials is not only dependent on the total surface porosity but also on the pore characteristics (morphology, shape, contour, area). When using sintered balls (Ball-Sint) with small and regular-shaped pores, the friction performance was similar to that of conventional dimple textured surfaces [75, 76]. Pores with dimensions smaller than the contact area and shallow depth (generally <0.5 μm) can also improve the hydrodynamic load-carrying capacity in non-conformal contacts due to the action of the so-called "micro-hydrodynamic bearing effect". The passage of the counter-body over the convergent region of the pores or textures can promote a local increment of the lubricant viscosity and pressure, thus increasing the hydrodynamic load capacity [3]. In addition, lubricant can be "sucked" into the texture or pore when the inlet pressure in the diverging region is lower than the ambient pressure [8, 9].

4.2 Laser textured samples

The Stribeck-like curves of the laser textured samples for SRR 100% are shown in **Figure 4**. Similar trends were also obtained for distinct SRRs. Since film thickness could not be measured for textured discs, COF results were plotted together with ECR values to highlight different lubrication regimes and lift-off speed.

Dimple-textured discs (Disc-Di) promoted friction reduction compared to the reference disc NP, especially at low speeds (<100 mm/s). Shallow radial grooves (Disc-G1) also slightly reduced friction compared to NP, whereas deeper textures (Disc-G2) produced significant higher COF. As previously demonstrated in [6, 75, 77] and observed in the present results, shallow features can boost the hydrodynamic load-carrying capacity in non-conformal EHD contacts due to the local increase in fluid pressure. On the contrary, deeper textures (Disc-G2) can disturb the lubricant film locally and, therefore, induce asperities contact and COF rise [77]. Considering the results of ECR and COF in **Figure 4**, this is following the behavior observed here. Boundary lubrication characterized by an ECR of 0% started roughly at the same speed for all samples (line "a" in **Figure 4**), whereas full-film EHD lubrication regime (ECR 100%) was achieved at different speeds (lines "b" and "c" in **Figure 4**). Dimples (Disc-Di) presented lower lift-off speed, having the steepest increase in ECR value and therefore film thickness and reaching hydrodynamic lubrication at the lowest speed. Dimples were followed by shallow radial grooves (Disc-G1), NP, and

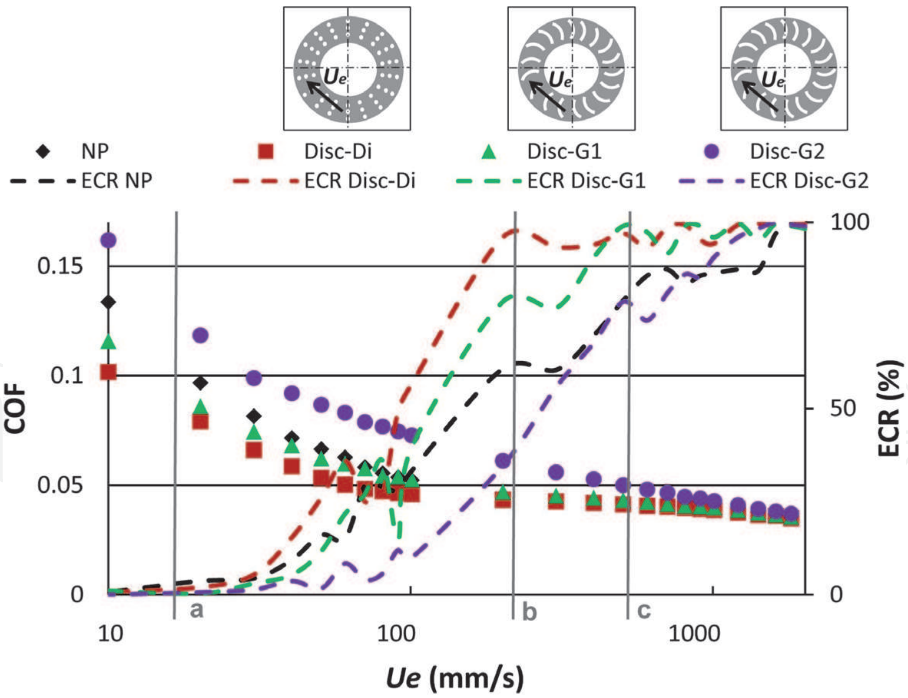

Figure 4.
Friction and contact resistance results of textured disc samples tested at SRR 100%.

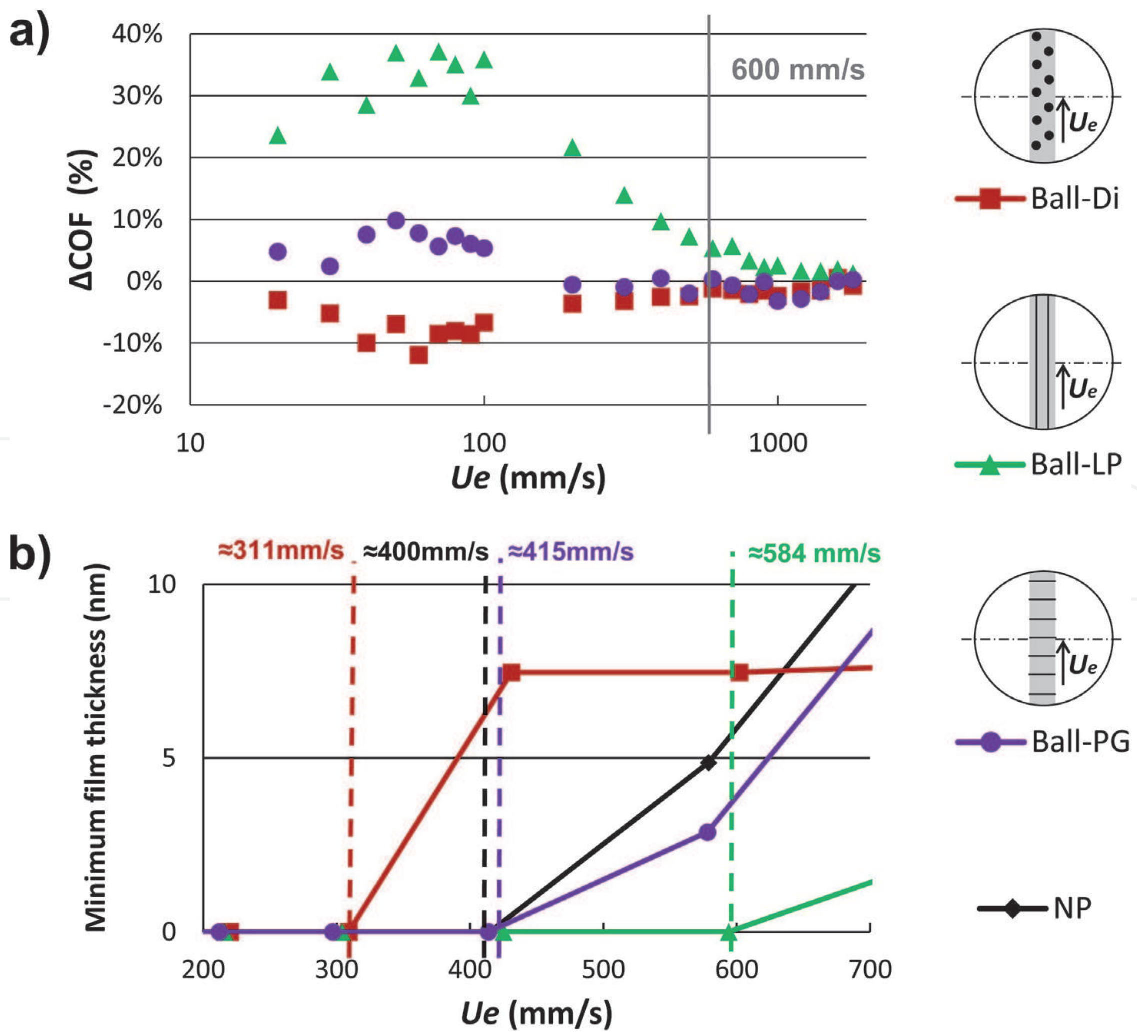

Figure 5.
a) Relative differences in friction plotted as a function of Ue using SRR 100% and b) measured minimum film thickness for NP and textured balls at low-speed (<800 mm/s) and lift-off speed values (vertical dashed lines).

finally deep radial grooves (Disc-G2). This trend proved that shallow configurations (Disc-Di and Disc-G1) had a micro-bearing effect under mixed lubrication, promoting full-film lubrication at lower speed than NP and Disc-G2, thus leading to reduced friction. This trend is also reflected in the COF *vs. Ue* dependence.

Results of textured balls were normalized using NP as a reference in **Figure 5a**, the negative values representing friction reduction. Differences between the samples are evident at *Ue* lower than 600 mm/s. Similarly to textured discs, the configuration of selected dimples (Ball-Di) improved frictional response. Perpendicular grooves (Ball-PG) generally behaved quite similarly to NP, whereas longitudinal grooves (Ball-LG) brought drawbacks and significantly increased COF. This behavior was observed for all the SRRs studied. To understand the reasons, film thickness results are presented in **Figure 5b**.

Particularly interesting are the values of minimum film thickness since the lift-off speed can be estimated from them. Comparing the different surface textures, dimples (Ball-Di) featured full-film conditions at a lower speed. Perpendicular grooves (Ball-PG) and NP showed similar lift-off speeds, whereas a complete separation between the rubbing surfaces was significantly delayed to higher speeds for longitudinal grooves (Ball-LG). COF and lift-off speed results are in good correlation, confirming the micro-bearing effect of dimples again. Perpendicular grooves did not significantly improve frictional performance, probably as a result of a great extent of the grooves in transversal direction (∼1 mm) relative to the contact dimensions (∼170 μm), leading to a reduction of pressure build-up as the lubricant flows transversally in the grooves upon contact with the counter body. Finally, longitudinal grooves (Ball-LG) did not improve the hydrodynamic load-carrying capacity, which can be traced back to a more effortless lubricant flow inside the grooves when the entrainment speed is in the direction of the textures. Upon contact, lubricant is thus squeezed out of the tribological contact, and the textures contribute to higher friction instead of local increment of pressure/ viscosity and film thickness [2, 12].

Sintered and textured samples were compared both from a manufacturing, topographical, and tribological point of view. The manufacturing of sintered materials inherently entails surface features that can potentially improve tribological performance. However, pores are randomly distributed, and the geometrical characteristics of the single features can only be influenced but not precisely tailored by the sintering parameters (**Table 2**). Furthermore, surface pores in sintered material increased surface roughness, making the direct geometrical and tribological comparison with smooth samples challenging (see **Figure 3**). On the other hand, the manufacturing of laser texturing requires extra effort, but it ensures a very precise tuning of the feature's geometry and distribution.

The topographical comparison between sintered and textured materials is quite demanding since the geometrical and spatial distributions of the features are significantly different. A series of parameters was selected to statistically compare the two classes of features, *i.e.* width *W* and depth *D* for dimension, area coverage *Ca* for spatial distribution, perpendicularity *P* and circularity *C* for shape, see **Table 3**. Only main representative parameters were selected here to reduce the complexity since they were also used as inputs for the ML model in the next section.

The tribological improvements of textured materials were observed in **Figures 4** and **5**. Particularly, dimple-configurations (Ball-Di and Disc-Di) reduced both COF and lift-off speed, increasing the load-carrying capacity compared to NP. Surface pores in sintered balls decreased friction compared to NP only at the same specific film thicknesses, see **Figure 3b**. The large difference in COF at equal entrainment speed between sintered and NP (see **Figure 3a**) is due to the extensive difference in surface roughness, see **Table 2**. Therefore, it should be noted that the presented pore configurations increased the lift-off speed since the increase of roughness requires higher speeds for reaching hydrodynamic conditions, see **Figure 3**. The tribological performances of dimples and pores in sintered balls can be comparable due to the geometrical similarities of surface features (see **Table 3**) and the small extent of cavities compared to the contact area.

A further comparison between sintered and textured materials is made in the following ML section. The geometrical parameters were used as inputs to characterize very different surfaces, and the COF was used as the output of the predicting model.

5. Machine learning approach

This preliminary model aims at predicting COF based on topographical characteristics of interfaces (surface pores and texture) rather than investigating the physical mechanisms associated to the tribological behavior.

The average coefficient of friction from 6228 experiments was organized in a training dataset of 1704 different combinations of geometric and operational parameters and, subsequently, used as inputs to a Hardy Multiquadric Radial Basis Function (RBF), as illustrated schematically in **Figure 6**. The mathematical development and detailed results are reported in [33]. Similar to several Artificial Neural Networks (ANN) methods, the RBF approach can produce a correct input–output mapping even for noisy and dispersed data. The RBF and experimental COF output were compared using the coefficient of determination (R^2) evaluation to avoid that the variation among the tribological experiments could be wrongly assessed as a surface feature or test parameter (*i.e.* overfitting). The results were considered satisfactory under this perspective because the error percentage was not significantly different from the maximum relative standard deviation of the dataset.

A summary of the model fitting capacity is shown in **Figure 7**, where the RBF and experimental COF results were plotted together. Overall, results from all the

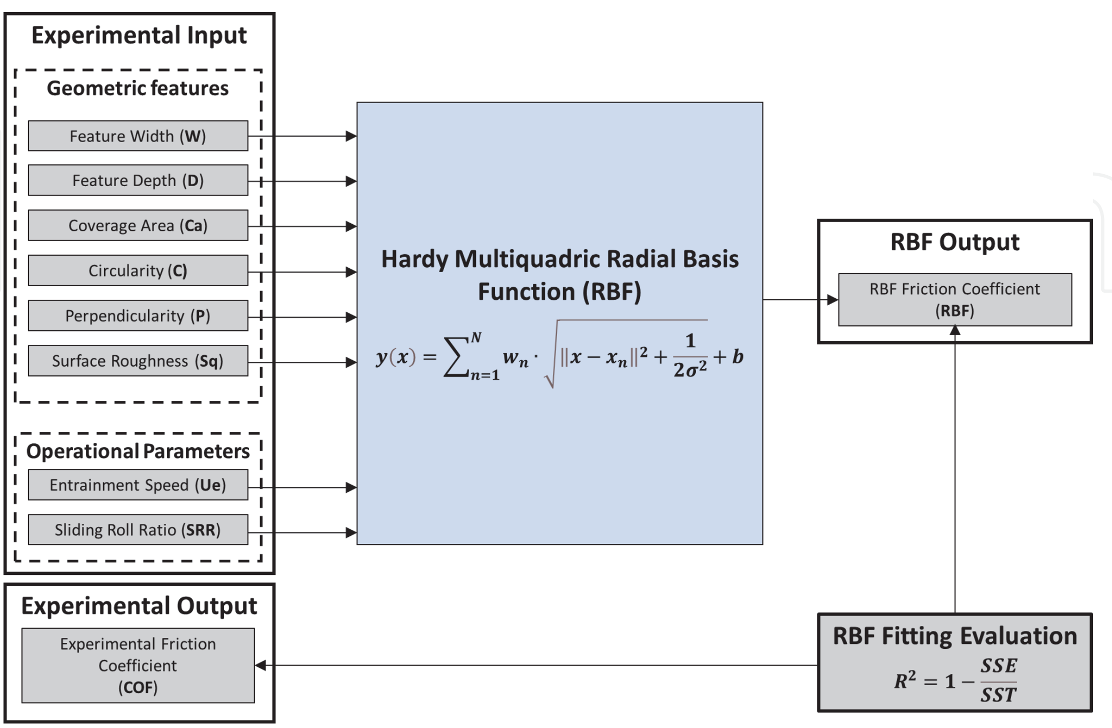

Figure 6.
Schematic of the machine learning model proposed to predict the frictional behavior of porous and textured interfaces from the experimental dataset.

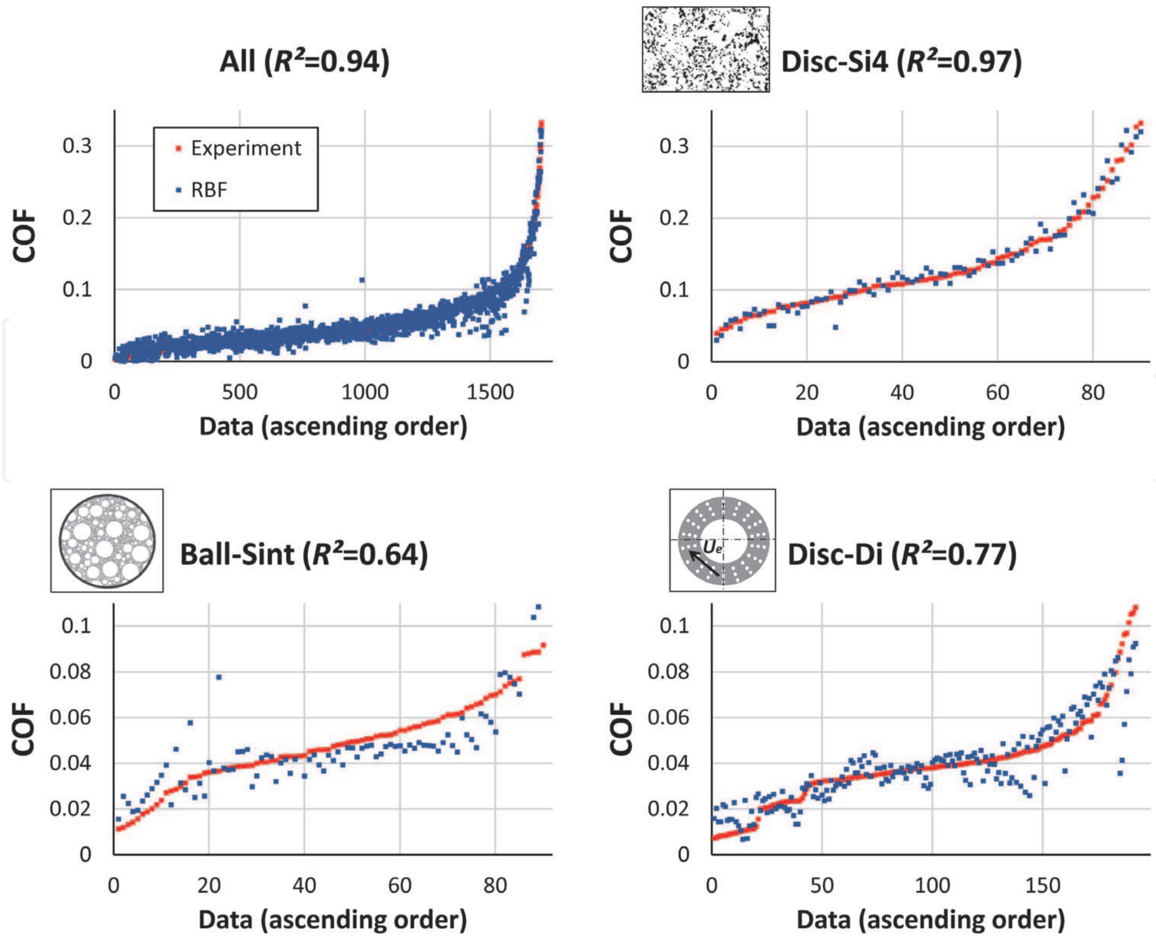

Figure 7.
Comparative plots for some surface features. Each number in the horizontal axis represents a single experimental test (single combination of surface and test parameters) sorted in ascending order according to friction results rather than in chronological order for improving readability.

different samples presented a high fitting capacity ($R^2 \approx 0.94$), being the worst Ball-Sint (≈0.64) and the best fitting Disc-Si4 (≈0.97). The R^2 values from the other surface configurations are distributed between these two extremity values.

The proposed model is more sensitive to high values of W, D and Ca. Low values of W and D for shallow configurations could be difficult to be interpreted by the model since the overall topography is not mathematically significantly different from the smooth samples NP. Furthermore, shallow features in Ball-Sint and Disc-Di also occupied a very small area (low Ca values), making it even more challenging to discern between NP and shallow features.

Together with the continuous improvement of the mathematical model and expansion of the dataset to shallow and less dense surfaces, these results indicate that the RBF methodology can be an effective tool for designing novel surface features for tribological applications.

6. Conclusions

The frictional performance of textured discs and balls containing surface pores or laser textures was assessed carrying out a wide range of experiments under lubricated non-conformal contact and varying kinematic conditions (speed and slide-to-roll-ratio).

Between the different texture geometries studied, dimples generally performed best, demonstrating the lowest COFs and lowest lift-off speed, which can be traced back to the increment of the hydrodynamic load-carrying capacity at lower speeds, further separating the rubbing surfaces and consequently reducing asperity contact. This was proven by film thickness and electric contact resistance measurements. Perpendicular grooves demonstrated beneficial performance compared with polished reference samples, depending on depth and transversal dimension. Potential beneficial effects of perpendicular grooves were partially mitigated by textures' excessive transversal dimension or depth. Longitudinal grooves led to unbeneficial tribological behavior, as equal entrainment and groove direction probably promoted lubricant migration out of the contact.

Sintering parameter tuning permitted to obtain different porosities and pore characteristics. The pore configuration achieved by machining the sintered ball samples reduced friction compared to the unstructured reference at the same specific film thickness.

Deterministic laser textures seem to outperform surface pores with random distribution and size despite the difficulties of comparing sintered with laser textured samples. This is particularly evident when considering the entrainment speed, showing that laser textures can significantly decrease the lift-off speed, after which full-film lubrication prevails by generating additional hydrodynamic pressure. Both textures have in common that textures of small dimensions being smaller than the contact area yielded the best results. However, it should be noted that laser texturing requires an additional manufacturing step, thus making the production process more complex.

Finally, considering that using advanced machine learning methods to describe tribological problems is still in its infancy, the proposed radial bias function approach showcased promising results that open new perspectives for its extension to support the optimum design of surface texturing for tribological applications in the future.

Acknowledgements

The State of São Paulo Research Foundation, Brazil (FAPESP grant N. 2016/25067-9), the Brazilian National Council for Scientific and Technological Development (CNPq) and the"Austrian COMET Program" (project InTribology, no. 872176) via the Austrian Research Promotion Agency (FFG) and the federal states of Niederösterreich and Vorarlberg are acknowledged for funding this work. Part of this work was carried out within the "Excellence Centre of Tribology" (AC2T research GmbH). C. Gachot acknowledges the government of Lower Austria for financially supporting the endowed professorship tribology at the TU Wien (Grant No. WST3-F-5031370/001–2017) in collaboration with AC2T research GmbH. D. Dini also acknowledges the support received from the Engineering and Physical Sciences Research Council (EPSRC) via his Established Career Fellowship EP/N025954/1. M. Roudrigues da Silva thanks the Centro Educacional da Fundação Salvador Arena and Termomecanica São Paulo S.A. for the financial support.

Author details

Guido Boidi[1*], Philipp G. Grützmacher[2], Markus Varga[1],
Márcio Rodrigues da Silva[3,4], Carsten Gachot[2], Daniele Dini[5], Francisco J. Profito[3]
and Izabel F. Machado[3]

1 AC2T research GmbH, Wiener Neustadt, Austria

2 Department of Engineering Design and Product Development, TU Wien, Austria

3 Polytechnic School, University of São Paulo – USP, São Paulo, Brazil

4 Faculdade de Tecnologia Termomecanica, São Bernardo do Campo, SP, Brazil

5 Department of Mechanical Engineering, Imperial College London, London, UK

*Address all correspondence to: guido.boidi@ac2t.at

References

[1] Lawrence KD, Ramamoorthy B. Multi-surface topography targeted plateau honing for the processing of cylinder liner surfaces of automotive engines. Appl Surf Sci 2016;365:19–30. https://doi.org/10.1016/j.apsusc.2015.12.245.

[2] Vlădescu SC, Olver A V., Pegg IG, Reddyhoff T. The effects of surface texture in reciprocating contacts - An experimental study. Tribol Int 2015;82:28–42. https://doi.org/10.1016/j.triboint.2014.09.015.

[3] Profito FJ, Vlădescu SC, Reddyhoff T, Dini D. Transient experimental and modeling studies of laser-textured micro-grooved surfaces with a focus on piston-ring cylinder liner contacts. Tribol Int 2017;113:125–136. https://doi.org/10.1016/j.triboint.2016.12.003.

[4] Rosenkranz A, Grützmacher PG, Gachot C, Costa HL. Surface Texturing in Machine Elements – A Critical Discussion for Rolling and Sliding Contacts. Adv Eng Mater 2019;1900194:1900194. https://doi.org/10.1002/adem.201900194.

[5] Rosenkranz A, Costa HL, Profito F, Gachot C, Medina S, Dini D. Influence of surface texturing on hydrodynamic friction in plane converging bearings - An experimental and numerical approach. Tribol Int 2019;134:190–204. https://doi.org/10.1016/j.triboint.2019.01.042.

[6] Wang X., Zhang H., Hsu SM. The Effects of dimple size and depth on friction reduction under boundary lubrication pressure 2007:24–26.

[7] Yu H, Wang X, Zhou F. Geometric shape effects of surface texture on the generation of hydrodynamic pressure between conformal contacting surfaces. Tribol Lett 2010;37:123–130. https://doi.org/10.1007/s11249-009-9497-4.

[8] Fowell M, Olver A V., Gosman AD, Spikes HA, Pegg I. Entrainment and inlet suction: Two mechanisms of hydrodynamic lubrication in textured bearings. J Tribol 2007;129:336–347. https://doi.org/10.1115/1.2540089.

[9] Olver A V., Fowell MT, Spikes HA, Pegg IG. "Inlet suction", a load support mechanism in non-convergent, pocketed, hydrodynamic bearings. Proc Inst Mech Eng Part J J Eng Tribol 2006;220:105–108. https://doi.org/10.1243/13506501JET168.

[10] Zimmer M, Vlădescu S-C, Mattsson L, Fowell M, Reddyhoff T. Shear-area variation: A mechanism that reduces hydrodynamic friction in macro-textured piston ring liner contacts. Tribol Int 2021;161:107067. https://doi.org/10.1016/j.triboint.2021.107067.

[11] Gropper D, Wang L, Harvey TJ. Hydrodynamic lubrication of textured surfaces: A review of modeling techniques and key findings. Tribol Int 2016;94:509–529. https://doi.org/10.1016/j.triboint.2015.10.009.

[12] Gachot C, Rosenkranz A, Hsu SM, Costa HL. A critical assessment of surface texturing for friction and wear improvement. Wear 2017;372–373:21–41. https://doi.org/10.1016/j.wear.2016.11.020.

[13] Sudeep U, Tandon N, Pandey RK. Performance of Lubricated Rolling/Sliding Concentrated Contacts With Surface Textures: A Review. J Tribol 2015;137:031501. https://doi.org/10.1115/1.4029770.

[14] Grützmacher PG, Profito FJ, Rosenkranz A. Multi-Scale Surface Texturing in Tribology — Current Knowledge and Future Perspectives. Lubricants 2019;7.

[15] Hamilton DB, Walowit JA, Allen CM. A Theory of Lubrication by Microirregularities. J Basic Eng 1966;88: 177–185. https://doi.org/10.1115/1.3645799.

[16] Anno JN, Walowit JA, Allen CM. Load Support and Leakage from Microasperity-Lubricated Face Seals. J Lubr Technol 1969;91:726–731. https://doi.org/10.1115/1.3555030.

[17] Etsion I, Burstein L. A Model for Mechanical Seals with Regular Microsurface Structure. Tribol Trans 1996;39:677–683. https://doi.org/10.1080/10402009608983582.

[18] Etsion I, Kligerman Y, Halperin G. Analytical and Experimental Investigation of Laser-Textured Mechanical Seal Faces. Tribol Trans 1999;42:511–516. https://doi.org/10.1080/10402009908982248.

[19] Kovalchenko A, Ajayi O, Erdemir A, Fenske G, Etsion I. The Effect of Laser Texturing of Steel Surfaces and Speed-Load Parameters on the Transition of Lubrication Regime from Boundary to Hydrodynamic. Tribol Trans 2004;47: 299–307. https://doi.org/10.1080/05698190490440902.

[20] Kovalchenko A, Ajayi O, Erdemir A, Fenske G, Etsion I. The effect of laser surface texturing on transitions in lubrication regimes during unidirectional sliding contact. Tribol Int 2005;38:219–225. https://doi.org/10.1016/j.triboint.2004.08.004.

[21] Pettersson U, Jacobson S. Influence of surface texture on boundary lubricated sliding contacts. Tribol Int 2003;36:857–864. https://doi.org/10.1016/S0301-679X(03)00104-X.

[22] Upadhyaya A, Upadhyaya GS. Powder Metallurgy: Science, Technology and Materials. First. Boca Raton, FL 33487, USA: CRC Press LLC, Taylor and Francis Group; 2011.

[23] Carabajar S, Verdu C, Hamel A, Fougères R. Fatigue behavior of a nickel alloyed sintered steel. Mater Sci Eng A 1998;257:225–234. https://doi.org/10.1016/S0921-5093(98)00846-6.

[24] Carabajar S, Verdu C, Fougères R. Damage mechanisms of a nickel alloyed sintered steel during tensile tests. Mater Sci Eng A 1997;232:80–87. https://doi.org/10.1016/S0921-5093(97)00100-7.

[25] Straffelini G, Molinari A, Danninger H. Impact notch toughness of high-strength porous steels. Mater Sci Eng A 1999;272:300–309. https://doi.org/10.1016/S0921-5093(99)00491-8.

[26] Straffelini G, Fontanari V, Molinari A. True and apparent Young's modulus in ferrous porous alloys. Mater Sci Eng A 1999;260:197–202. https://doi.org/10.1016/S0921-5093(98)00960-5.

[27] Martin F, García C, Blanco Y. Influence of residual porosity on the dry and lubricated sliding wear of a powder metallurgy austenitic stainless steel. Wear 2015;328–329:1–7. https://doi.org/10.1016/j.wear.2015.01.025.

[28] Li X, Olofsson U. A study on friction and wear reduction due to porosity in powder metallurgic gear materials. Tribol Int 2017;110:86–95. https://doi.org/10.1016/j.triboint.2017.02.008.

[29] Boidi G, Profito FJ, Kadiric A, Machado IF, Dini D. The use of Powder Metallurgy for promoting friction reduction under sliding-rolling lubricated conditions. Tribol Int 2021; 157:106892. https://doi.org/10.1016/j.triboint.2021.106892.

[30] Rosenkranz A, Marian M, Profito FJ, Aragon N, Shah R. The Use of Artificial Intelligence in Tribology—A Perspective. Lubricants 2020;9:2. https://doi.org/10.3390/lubricants9010002.

[31] Prost J, Cihak-Bayr U, Neacşu IA, Grundtner R, Pirker F, Vorlaufer G.

Semi-Supervised Classification of the State of Operation in Self-Lubricating Journal Bearings Using a Random Forest Classifier. Lubricants 2021;9:50. https://doi.org/10.3390/lubricants9050050.

[32] Pandiyan V, Prost J, Vorlaufer G, Varga M, Wasmer K. Identification of abnormal tribological regimes using a microphone and semi-supervised machine-learning algorithm. Friction 2021. https://doi.org/10.1007/s40544-021-0518-0.

[33] Boidi G, da Silva MR, Profito FJ, Machado IF. Using Machine Learning Radial Basis Function (RBF) Method for Predicting Lubricated Friction on Textured and Porous Surfaces. Surf Topogr Metrol Prop 2020;8:044002. https://doi.org/10.1088/2051-672X/abae13.

[34] German RM. Sintering Theory and Practice. Ed. John Wiley and Sons: 1996.

[35] Barsoum MW. Fundamentals of ceramics. The Mc Graw-Hill Companies Inc.: 2003.

[36] Chen W, Anselmi-Tamburini U, Garay JE, Groza JR, Munir ZA. Fundamental investigations on the spark plasma sintering/synthesis process: I. Effect of dc pulsing on reactivity. Mater Sci Eng A 2005;394:132–138. https://doi.org/10.1016/j.msea.2004.11.020.

[37] Fukumasu NK, Boidi G, Seriacopi V, Machado GAA, Souza RM, Machado IF. Numerical analyses of stress induced damage during a reciprocating lubricated test of fecmo sps sintered alloy. Tribol Int 2017;113:443–447. https://doi.org/10.1016/j.triboint.2016.12.025.

[38] Balima F, Largeteau A. Phase transformation of alumina induced by high pressure spark plasma sintering (HP-SPS). Scr Mater 2019;158:20–23. https://doi.org/10.1016/j.scriptamat.2018.08.016.

[39] Fu L, Wu C, Grandfield K, Unosson E, Chang J, Engqvist H, et al. Transparent single crystalline ZrO2-SiO2 glass nanoceramic sintered by SPS. J Eur Ceram Soc 2016;36:3487–3494. https://doi.org/10.1016/j.jeurceramsoc.2016.05.016.

[40] Xuan CJ, Zhao Z, Jönsson PG. Wettability and corrosion of spark plasma sintered (SPS) ZrN by liquid iron and steel. J Eur Ceram Soc 2016;36:2435–2442. https://doi.org/10.1016/j.jeurceramsoc.2016.03.006.

[41] Boidi G, Fukumasu NK, Machado IF. Wear and friction performance under lubricated reciprocating tests of steel powder mixtures sintered by Spark Plasma Sintering. Tribol Int 2018;121:139–147. https://doi.org/10.1016/j.triboint.2018.01.032.

[42] Zhan G-D, Kuntz J, Wan J, Garay J, Mukherjee AK. A Novel Processing Route to Develop a Dense Nanocrystalline Alumina Matrix (<100 nm) Nanocomposite Material. J Am Ceram Soc 2003;86:200–2002. https://doi.org/10.1111/j.1151-2916.2003.tb03306.x.

[43] Omori M. Sintering, consolidation, reaction and crystal growth by the spark plasma system (SPS). Mater Sci Eng A 2000;287:183–188. https://doi.org/10.1016/s0921-5093(00)00773-5.

[44] Li W, Gao L. Fabrication of HAp-ZrO2 (3Y) nano-composite by SPS. Biomaterials 2003;24:937–940. https://doi.org/10.1016/S0142-9612(02)00428-3.

[45] Zarebski K, Putyra P. Iron powder-based graded products sintered by conventional method and by SPS. Adv Powder Technol 2015;26:401–408. https://doi.org/10.1016/j.apt.2014.11.010.

[46] Orrù R, Licheri R, Locci AM, Cincotti A, Cao G. Consolidation/synthesis of materials by electric current

activated/assisted sintering. Mater Sci Eng R Reports 2009;63:127–287. https://doi.org/10.1016/j.mser.2008.09.003.

[47] Machado IF, Girardini L, Lonardelli I, Molinari A. The study of ternary carbides formation during SPS consolidation process in the WC–Co–steel system. Int J Refract Met Hard Mater 2009;27:883–891. https://doi.org/10.1016/J.IJRMHM.2009.05.001.

[48] Li X, Olofsson U, Bergseth E. Pin-on-Disc Study of Tribological Performance of Standard and Sintered Gear Materials Treated with Triboconditioning Process: Pretreatment by Pressure-Induced Tribofilm Formation. Tribol Trans 2017;60:47–57. https://doi.org/10.1080/10402004.2016.1146379.

[49] Li X, Sosa M, Olofsson U. A pin-on-disc study of the tribology characteristics of sintered versus standard steel gear materials. Wear 2014;340–341:31–40. https://doi.org/10.1016/j.wear.2015.01.032.

[50] Dlapka M, Danninger H, Gierl C, Lindqvist B. Defining the pores in PM components. Met Powder Rep 2010;65:30–33. https://doi.org/10.1016/S0026-0657(10)70093-X.

[51] Schneider CA, Rasband WS, Eliceiri KW. NIH Image to ImageJ: 25 years of image analysis. Nat Methods 2012;9:671–675. https://doi.org/10.1038/nmeth.2089.

[52] Seville J.P.K.;, Wu CY. Particle Technology and Engineering: an Engineer's Guide to Particles and Powders: Fundamentals and Computational Approaches. 2016.

[53] Grabon W, Pawlus P, Wos S, Koszela W, Wieczorowski M. Effects of cylinder liner surface topography on friction and wear of liner-ring system at low temperature. Tribol Int 2018;121:148–160. https://doi.org/10.1016/j.triboint.2018.01.050.

[54] Reizer R, Pawlus P. 3D surface topography of cylinder liner forecasting during plateau honing process. J Phys Conf Ser 2011;311:012021. https://doi.org/10.1088/1742-6596/311/1/012021.

[55] Grabon W, Pawlus P, Wos S, Koszela W, Wieczorowski M. Effects of honed cylinder liner surface texture on tribological properties of piston ring-liner assembly in short time tests. Tribol Int 2017;113:137–148. https://doi.org/10.1016/j.triboint.2016.11.025.

[56] Boidi G. An experimental assessment of surface micro irregularities (porosity and texture) effects on tribological behavior under lubricated conditions. Doctorate Thesis, Universidade de São Paulo, 2019. https://doi.org/10.11606/T.3.2019.tde-22102019-091137.

[57] Boidi G, Tertuliano IS, Cano MF, Machado GAA, Souza RM, Machado IF. Tribological Evaluation of Sintered and Conventional Gear Materials, 2017. https://doi.org/10.4271/2017-36-0153.

[58] Boidi G, Tertuliano IS, Lima LGBS, Profito FJ, Machado IF. Porosity Effect of Sintered Steel on the Frictional Performance of Conformal and Nonconformal Lubricated Contacts. Tribol Trans 2019;62:1029–1040. https://doi.org/10.1080/10402004.2019.1640917.

[59] Costa H, Hutchings I. Some innovative surface texturing techniques for tribological purposes. Proc Inst Mech Eng Part J J Eng Tribol 2015;229:429–448. https://doi.org/10.1177/1350650114539936.

[60] Chichkov BN, Momma C, Nolte S, Alvensleben F, Tünnermann A. Femtosecond, picosecond and nanosecond laser ablation of solids. Appl Phys A Mater Sci Process 1996;63:109–115. https://doi.org/10.1007/BF01567637.

[61] Grützmacher PG, Rosenkranz A, Szurdak A, Gachot C, Hirt G,

Mücklich F. Lubricant migration on stainless steel induced by bio-inspired multi-scale surface patterns. Mater Des 2018;150:55–63. https://doi.org/10.1016/j.matdes.2018.04.035.

[62] Grützmacher PG, Rosenkranz A, Szurdak A, König F, Jacobs G, Hirt G, et al. From lab to application - Improved frictional performance of journal bearings induced by single- and multi-scale surface patterns. Tribol Int 2018; 127:500–508. https://doi.org/10.1016/j.triboint.2018.06.036.

[63] Mücklich F, Lasagni A, Daniel C. Laser Interference Metallurgy – using interference as a tool for micro/nano structuring. Int J Mater Res 2006;97: 1337–1344. https://doi.org/10.3139/146.101375.

[64] Heemskerk RS, Vermeiren KN, Dolfsma H. Measurement of Lubrication Condition in Rolling Element Bearings. A S L E Trans 1982;25:519–527. https://doi.org/10.1080/05698198208983121.

[65] Luo J, Wen S, Huang P. Thin film lubrication. Part I. Study on the transition between EHL and thin film lubrication using a relative optical interference intensity technique. Wear 1996;194:107–115. https://doi.org/10.1016/0043-1648(95)06799-X.

[66] Cann PM, Spikes HA, Hutchinson J. The development of a spacer layer imaging method (slim) for mapping elastohydrodynamic contacts. Tribol Trans 1996;39:915–921. https://doi.org/10.1080/10402009608983612.

[67] Johnston GJ, Wayte R, Spikes HA. The measurement and study of very thin lubricant films in concentrated contacts. Tribol Trans 1991;34:187–194. https://doi.org/10.1080/10402009108982026.

[68] Guégan J. Experimental Investigation into the Influence of Roughness on Friction and Film Thickness in EHD Contacts. Imperial College London, 2015. https://doi.org/10.25560/53388.

[69] Guegan J, Kadiric A, Spikes H. A Study of the Lubrication of EHL Point Contact in the Presence of Longitudinal Roughness. Tribol Lett 2015;59:1–18. https://doi.org/10.1007/s11249-015-0549-7.

[70] Guegan J, Kadiric A, Gabelli A, Spikes H. The Relationship Between Friction and Film Thickness in EHD Point Contacts in the Presence of Longitudinal Roughness. Tribol Lett 2016;64:1–15. https://doi.org/10.1007/s11249-016-0768-6.

[71] Rycerz P, Kadiric A. The Influence of Slide–Roll Ratio on the Extent of Micropitting Damage in Rolling–Sliding Contacts Pertinent to Gear Applications. Tribol Lett 2019;67:63. https://doi.org/10.1007/s11249-019-1174-7.

[72] Boidi G, Grützmacher PG, Kadiric A, Profito FJ, Machado IF, Gachot C, et al. Fast laser surface texturing of spherical samples to improve the frictional performance of elasto-hydrodynamic lubricated contacts. Friction 2021;9:1227–1241. https://doi.org/10.1007/s40544-020-0462-4.

[73] Boidi G, Tertuliano IS, Profito FJ, de Rossi W, Machado IF. Effect of laser surface texturing on friction behavior in elastohydrodynamically lubricated point contacts under different sliding-rolling conditions. Tribol Int 2020;149: 105613. https://doi.org/10.1016/j.triboint.2019.02.021.

[74] Li S, Parmar U. The Effects of Microdimple Texture on the Friction and Thermal Behavior of a Point Contact. J Tribol 2018;140:041503. https://doi.org/10.1115/1.4039228.

[75] Krupka I, Hartl M, Zimmerman M, Houska P, Jang S. Effect of surface

texturing on elastohydrodynamically lubricated contact under transient speed conditions. Tribol Int 2011;44:1144–1150. https://doi.org/10.1016/j.triboint.2011.05.005.

[76] Mourier L, Mazuyer D, Ninove FP, Lubrecht AA. Lubrication mechanisms with laser-surface-textured surfaces in elastohydrodynamic regime. Proc Inst Mech Eng Part J J Eng Tribol 2010;224:697–711. https://doi.org/10.1243/13506501JET771.

[77] Mourier L, Mazuyer D, Lubrecht AA, Donnet C. Transient increase of film thickness in micro-textured EHL contacts. Tribol Int 2006;39:1745–1756. https://doi.org/10.1016/j.triboint.2006.02.037.